scientific reports

Check for updates

OPEN

# Structural analysis of Si-doped amorphous $In_2O_3$ based on quantum beam measurements and computer simulations

Yuta Shuseki[1,2], Akihiko Fujiwara[3]✉, Nobuhiko Mitoma[4], Takio Kizu[4], Toshihide Nabatame[4], Kazuhito Tsukagoshi[4], Yohei Onodera[2], Atsunobu Masuno[1,2], Koji Ohara[5,6] & Shinji Kohara[2]✉

**The structural properties and thermal stability of Si-doped amorphous indium oxide (ISO) were investigated via experimental characterization and computational modeling techniques. The total structure factors, $S(Q)$, and reduced pair distribution functions, $G(r)$, were calculated for both annealed and pristine ISO samples, revealing the distinct structural features induced by Si doping and thermal treatment. Although the pristine ISO samples exhibited halo patterns indicative of an amorphous structure, annealing at 600 °C led to pronounced Bragg peaks, suggesting that the sample was crystallized. However, an ISO with a higher Si content (20 at%) retained its amorphous structure even after annealing, highlighting the role of Si-doping in enhancing the thermal stability. Classical molecular dynamics–reverse Monte Carlo simulations were employed to elucidate the structure of pristine ISO samples, revealing good agreement with the experimental data. Furthermore, the partial structure factors, $S_{ij}(Q)$, and partial pair distribution functions, $g_{ij}(r)$ demonstrate the influence of Si doping on atomic correlations and density changes in the ISO. Polyhedral connectivity analysis suggests that the fraction changes of edge sharing due to Si doping affect the thermal stability of ISO and that $SiO_4$ tetrahedra play a crucial role in inhibiting crystallization.**

**Keywords** Amorphous indium oxide, X-ray diffraction, Molecular dynamics simulation, Reverse Monte Carlo, Topological analysis, Thermal stability

Energy consumption has reached unprecedented levels owing to the proliferation of devices with semiconductors connected to daily applications (Internet of Things), and computers are being used in various situations. To address these energy problems, thin films of metal oxide semiconductors and conductors are garnering attention[1,2]. In particular, thin films of indium oxide ($In_2O_3$) are widely recognized for their low electrical resistance ($\rho = \sim 10^{-4}$ Ωcm) as a conductor and large band gap ($E_g = 3.36$) as a semiconductor[3–5]. In addition, these thin-film semiconductors exhibit high carrier mobility and high transparency within the visible light range, making them suitable as both conducting electrodes and semiconductor active layers[6,7]. Historically, expensive single-crystal Si has been used as a channel material for thin-film transistors (TFTs). In contrast, employing cheaper polycrystalline or amorphous Si (*a*-Si) results in a significant decrease in carrier mobility, leading to poor performance[8]. Many studies have focused on amorphous oxide semiconductors, highlighting the high mobility and transparency of materials such as amorphous In–Zn–O (*a*-IZO)[9,10] and amorphous In–Ga–Zn–O (*a*-IGZO)[11–13]. Although *a*-IGZO exhibits higher electron mobility than *a*-Si TFTs, the structural stability of *a*-IGZO is lacking. Conversely, amorphous Si-doped $In_2O_3$, amorphous In–Si–O (*a*-ISO), has been reported to exhibit higher structural stability than *a*-IGZO[14–17].

High-energy X-ray diffraction (HEXRD)[18] is considered to be a suitable method for understanding the atomic structures of various materials, including crystals[19,20] liquids[21,22] and amorphous materials[23,24]. Particularly for liquids and amorphous materials lacking long-range structural information, HEXRD over a wide $Q$ range is

[1]Graduate School of Engineering, Kyoto University, Kyoto 615-8520, Japan. [2]Center for Basic Research on Materials, National Institute for Materials Science (NIMS), Tsukuba, Ibaraki 305-0047, Japan. [3]School of Engineering, Kwansei Gakuin University, Sanda, Hyogo 669-1330, Japan. [4]Research Center for Materials Nanoarchitectonics (MANA), National Institute for Materials Science (NIMS), Tsukuba, Ibaraki 305-0044, Japan. [5]Faculty of Materials for Energy, Shimane University, Matsue 690-8504, Shimane, Japan. [6]Diffraction and Scattering Division, Synchrotron Radiation Research Institute (JASRI), Sayo-gun, Hyogo 679–5198, Japan. ✉email: akihiko.fujiwara@kwansei.ac.jp; KOHARA.Shinji@nims.go.jp

essential for obtaining accurate pair distribution functions, $g(r)$[25]. In addition, the combination of quantum beam measurements and computer simulations is a well-known approach for elucidating atomic structures in greater detail. Classical molecular dynamics (CMD) and density functional theory (DFT) are commonly used for modeling inorganic materials[26,27] offering methods for generating three-dimensional structures and understanding various features such as atomic distances, bond angles, and electronic states. Previous studies have employed simulation techniques to investigate *a*-$In_2O_3$[28,29]. Alternatively, the reverse Monte Carlo (RMC) method can be used to generate structures based on experimental data obtained from quantum beam measurements. Numerous studies have utilized RMC modeling for materials such as $SiO_2$ glass[30] $Ge_2Se_2$ glass[31] and amorphous alloys[32].

It is suggested from previous reports that Si-doped enhances the structural stability of amorphous $In_2O_3$, but the reason for this phenomenon is not well understood. The structural change of $InO_x$–$InO_x$ induced by Si-doping likely contributes to the structural stability. In particular, the structural comparison between Si-doped $In_2O_3$ and crystalline $In_2O_3$ is a key point to elucidate the structural stabilization. In this study, we aimed to clarify the thermal stability of Si-doped ISO by utilizing structural models derived from CMD–RMC modeling based on data from quantum beam measurements. Specifically, we attempted to understand how the structural changes induced by Si doping affected the thermal stability.

## Experimental and simulation procedures

### Sample preparation

ISO thin films were formed on a quartz substrate (100 mm×100 mm) covered by a poly (methyl methacrylate) resist using a DC magnetron sputtering system (Shibaura Mechatronics, CFS-4EP-LL i-Miller) at room temperature. The three-inch sputtering targets composed of $In_2O_3$ and $SiO_2$ with Si concentrations, Si/(In + Si), of 0, 2, 7, 11, and 20 at% were used. The sputtering targets and substrates in the sputtering system were 160 mm apart. DC sputtering was performed at a power of 200 W under an Ar and $O_2$ mixed atmosphere with an Ar: $O_2$ gas flow ratio of 1:1 at a total pressure of 0.25 Pa[17]. After the thin films were formed, they were removed from the substrate by soaking in acetone. The removed thin films were encapsulated in glass capillaries. The as-grown samples and those annealed at 600 °C in a muffle furnace were used for the HEXRD measurements.

### HEXRD

The HEXRD measurements were conducted on the BL04B2 beamline[33] of SPring-8 in Japan, utilizing an energy of 61.4 keV. The obtained data were normalized, including adjustments for polarization, absorption, background, and Compton scattering, using the original software[33] of the BL04B2 beamline. Subsequently, all data were normalized to Faber–Ziman total structure factors, $S(Q)$[34].

$$S(Q) = 1 + \frac{1}{|<w(Q)>|^2} \sum_{\alpha} \sum_{\beta} c_\alpha c_\beta w_\alpha^*(Q) w_\beta(Q) [S_{\alpha\beta}(Q) - 1], \tag{1}$$

where $Q$ is the magnitude of the scattering vector, $c_\alpha$ is the atomic fraction of chemical species $\alpha$, $w_\alpha$ is the atomic form factor with dispersion terms for chemical species $\alpha$ and is, in general, a complex number, $S_{\alpha\beta}(Q)$ is the partial structure factor, and $|<w(Q)>|$ is calculated according to the method described in Eq. (2).

$$|<w(Q)>|^2 = \sum_{\alpha} \sum_{\beta} c_\alpha c_\beta w_\alpha^*(Q) w_\beta(Q). \tag{2}$$

The reduced pair distribution function, $G(r)$, was obtained using the Fourier transform of $S(Q)$.

$$G(r) = \frac{2}{\pi} \int_{Q_{\min}}^{Q_{\max}} Q[S(Q) - 1] \sin(Qr)\, dQ. \tag{3}$$

Hence, Eq. (3) can be converted as follows.

$$g(r) = \frac{G(r)}{4\pi r \rho_0} + 1, \tag{4}$$

$$g(r) = \frac{\rho(r)}{\rho_0}, \tag{5}$$

where $\rho_0 = N/V$, N/V is the number of atoms in the volume V and $\rho(r)$ is a density at distance $r$. The number density can be calculated from the value of the minimum of $G(r)/4\pi r$ in Eq. (6)[35].

$$\left| \left\{ \frac{G(r)}{4\pi r} \right\}_{min}^{r \geq r_{min}} \right| = |\rho(r) - \rho_0| \approx \rho_0. \tag{6}$$

The accuracy of this method using $SiO_2$ glass is summarized in Fig. S1. The density of $SiO_2$ glass is 2.20 g/cm$^3$, while our estimated value is 2.27 g/cm$^3$. The error of the density was estimated to be 3.1%.

Table 1 summarizes the target concentration and the estimated density data from $G(r)$ for ISO.

| | Targeted concentrations of ISO | | | |
|---|---|---|---|---|
| | In | Si | O | Estimated density from G(*r*) |
| ISO0 ($In_2O_3$) | 2.00 | 0 | 3.00 | 6.28 |
| ISO2 | 39.00 | 1.00 | 60.00 | 6.18 |
| ISO7 | 36.84 | 2.63 | 60.53 | 6.09 |
| ISO11 | 34.91 | 4.24 | 60.85 | 5.92 |
| ISO20 | 30.58 | 7.85 | 61.57 | 5.84 |

**Table 1**. Composition and estimated density of Si-doped amorphous $In_2O_3$.

| | $A_{ij}$ / J | $B_{ij}$ / Å$^{-1}$ |
|---|---|---|
| In–O | $2.47 \times 10^{-14}$ | 5.50 |
| In–In | $5.30 \times 10^{-16}$ | 3.00 |
| O–O | $2.71 \times 10^{-16}$ | 3.00 |
| Si–O | $1.01 \times 10^{-14}$ | 6.06 |

**Table 2**. Potential parameter for classical molecular dynamics simulation of BMH.

## Structural modeling and analysis

Computational structural modeling was performed using CMD and RMC modeling. The generation of the initial configurations, CMD, was employed with the Born–Mayer–Huggins (BMH)[36] force field utilizing the potential parameters reported by Utsuno et al.[37]. In addition, we used the $SiO_2$ potential parameter reported by Zhen et al.[38]. The equations and parameters are detailed in Eq. (7) and are listed in Table 2. Although we evaluated various parameters[37,39] in Fig. S2, none showed significant differences. We ultimately chose the potential parameters of Utsuno et al. because their data were based on amorphous thin $In_2O_3$ films.

$$\Phi_{ij} = \frac{e^2}{4\pi\epsilon_0}\frac{Z_i Z_j}{r_{ij}} + A_{ij}\exp\left(-B_{ij}r_{ij}\right), \tag{7}$$

where $e$ is the elementary charge, $r_{ij}$ is the distance between $i$ and $j$ atoms, $Z_i$ is the electronic charge of the $i$ atom ($Z_{In} = +3.0$, $Z_O = -2.0$, $Z_{Si} = +4.0$), and $A_{ij}$ and $B_{ij}$ are parameters for the $i$–$j$ pair. Periodic boundary conditions were employed in the simulation and long-range Coulombic interactions were calculated using the Ewald method. When combining the potentials derived from different sources, variations in the parameters can affect the results, and thus, we compared the $S(Q)$ and $G(r)$ curve obtained using CMD and CMD–RMC to evaluate the effect of mixing the potentials (Fig. S3). No unnatural changes or unrealistic structures are observed with increasing amounts of Si doping. Furthermore, upon comparing the coordination numbers of the structures obtained using the CMD and CMD–RMC models (Table S1), the difference in the most important In–O coordination number is extremely small (approximately 1%). Additionally, the differences in the coordination numbers of In–In and O–O are limited to approximately 3% and 1%, respectively. Even the differences in the coordination numbers of ISO0, which does not contain Si, and ISO2–20, which contain Si, are minimal, confirming that the influences of the differences in the potentials on the structure are limited. These results suggest that the framework structure is determined via CMD in this study, and modifications via RMC are mainly limited to the fine tuning of the long-range structure. Therefore, the topological characteristics of the amorphous structure remain essentially unchanged. A cubic cell contains approximately 10,000 atoms arranged randomly (In: 4000, O: 6000 for ISO0, In: 3900, Si: 100, O: 6050 for ISO2, In:3684, Si:263, O: 6052 for ISO7, In:3492, Si:424, O:6086 for ISO11, and In:3058, Si:785, O:6157 for ISO20) in the initial configuration. CMD simulations were performed in the NVT ensemble after annealing for 100 ps at 1000 K, cooling at a rate of 97 K/ps from 1000 to 300 K, and equilibration at 300 K for 10 ps. The CMD simulations were conducted using the LAMMPS program[40]. Following the CMD simulation, RMC modeling utilizing the RMC++code[41] was used to refine the structure based on the HEXRD experimental data.

The coordination numbers and polyhedral connectivity were computed using the original program with the first coordination distances of In–In: 4.50 Å, In–O: 2.8 Å, Si–O: 1.9 Å and O–O: 4.00 Å, respectively. In addition, the king ring size distribution was calculated using the R.I.N.G.S. code[42]. The reduced pair distribution functions, $G(r)$, of the crystalline $In_2O_3$ was calculated using PDFgui[43].

## Results and discussion

### High energy X-ray diffraction data of ISO

Figure 1 (left) shows the total structure factors, $S(Q)$, of both annealed (red line) and pristine (black line) ISO0, 2, 7, 11, and 20. The pristine ISO samples, except ISO0, exhibited a halo pattern, which is characteristic of an amorphous structure. This behavior suggests that Si doping more readily induces the formation of an amorphous structure in the ISO. In contrast, ISO0, 2, 7, and 11 annealed at 600 °C exhibited pronounced Bragg peaks,

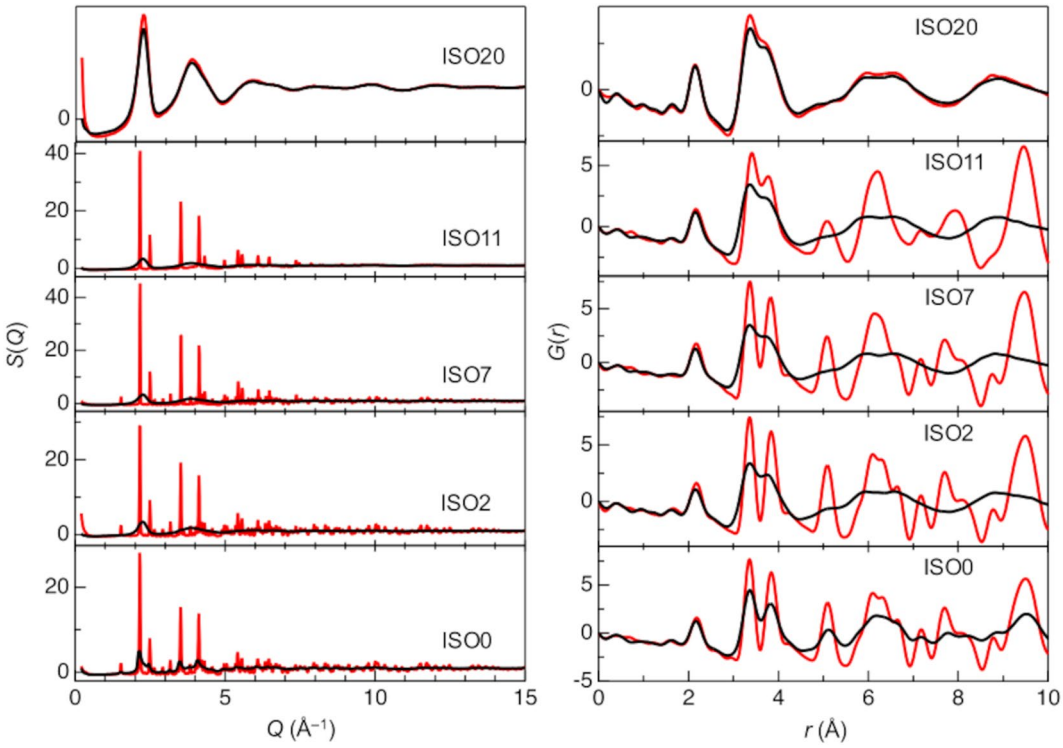


**Fig. 1**. X-ray total structure factors, $S(Q)$, and reduced pair distribution functions, $G(r)$, of pristine and annealed ISO0, 2, 7, 11, and 20. Black line, pristine samples; red line, annealed samples.

indicating crystallization of the samples due to thermal treatment. However, only ISO20 retained its amorphous structure at temperatures above 600 °C, suggesting that over 20 at% Si doping is necessary to maintain an amorphous structure during the thermal treatment of ISO. The reduced pair distribution functions, $G(r)$, of both annealed and pristine ISO0, 2, 7, 11, and 20 are shown in Fig. 1 (right). While all the peaks are located at similar $r$ positions, the annealed samples exhibit peaks attributed to the improved periodicity. Consequently, the $G(r)$ around long ranges (over 5.00 Å) of annealed ISO0, 2, 7, and 11 (crystalline) shows more obvious peaks compared to the amorphous ones. These peaks reveal atomic correlations, such as In–O (2.10 Å) and In–In/O–O (ranging from 3.20 to 3.90 Å). Figure S4, in which $G(r)$ was calculated using crystal structures from previous research[44,45] shows that all samples transitioned to cubic $In_2O_3$ after annealing, in contrast to the cubic, trigonal, and orthorhombic $G(r)$ structures of crystalline $In_2O_3$. Typically, Si atoms form $SiO_4$ tetrahedra in amorphous samples, with an Si–O distance of approximately 1.60 Å. However, the $G(r)$ data for all samples did not clearly exhibit Si–O peaks because X-rays are scattered by electron clouds, so the scattering ability varies depending on the atomic species (number of electrons). We calculated the approximate X-ray weighting factors, $W_{ij}$, using Eq. (1) for ISO20. In the case of X-rays, owing to the $Q$-dependence of the atomic form factor, $f(Q)$, the weighting factors cannot be expressed as constants. Therefore, in Eq. (8), the weighting factors are calculated using the atomic numbers,

$$\begin{aligned} S(Q) =& 0.509 S_{\mathrm{In-In}}(Q) + 0.334 S_{\mathrm{In-O}}(Q) + 0.075 S_{\mathrm{In-Si}}(Q) \\ &+ 0.055 S_{\mathrm{O-O}}(Q) + 0.025 S_{\mathrm{Si-O}}(Q) + 0.003 S_{\mathrm{Si-Si}}(Q), \end{aligned} \tag{8}$$

The weighting factors for the In–Si, Si–O, and Si–Si correlations were very small compared to those for the In–In or In–O correlations. Therefore, our data did not show clear Si–In, Si–O, or Si–Si peaks. We calculated the estimated density values of amorphous ISO2, 7, 11, and 20 samples from the slope of $G(r)$ in the range of 0–1.30 Å (Table 1), and we utilized these values for the MD–RMC simulations[46].

## Structural modeling

In this study, we only developed structural models for pristine ISO2, 7, 11, and 20 because our objective was to elucidate the thermal stability of Si-doped amorphous ISO. The structural modeling of pristine ISO2, 7, 11, and 20 was conducted using CMD simulations (Fig. S2). While good agreement was found between the experimental and simulated $S(Q)$ data, the simulation data of $G(r)$ beyond 5.00 Å shifted to higher $r$ compared to the experimental data. It is suggested that this discrepancy arose from the force field potentials, as the potential of Utsuno et al. was adjusted using a density value of 7.10 g/cm$^3$ for amorphous $In_2O_3$, which is higher than the estimated density of our samples (approximately 6.00 g/cm$^3$). Therefore, the CMD simulation was employed to make an initial configuration for the RMC refinement. Figure 2 shows the total structure factors, $S(Q)$, and the reduced pair distribution functions, $G(r)$, for the ISO2, 7, 11, and 20 samples. The agreement between the

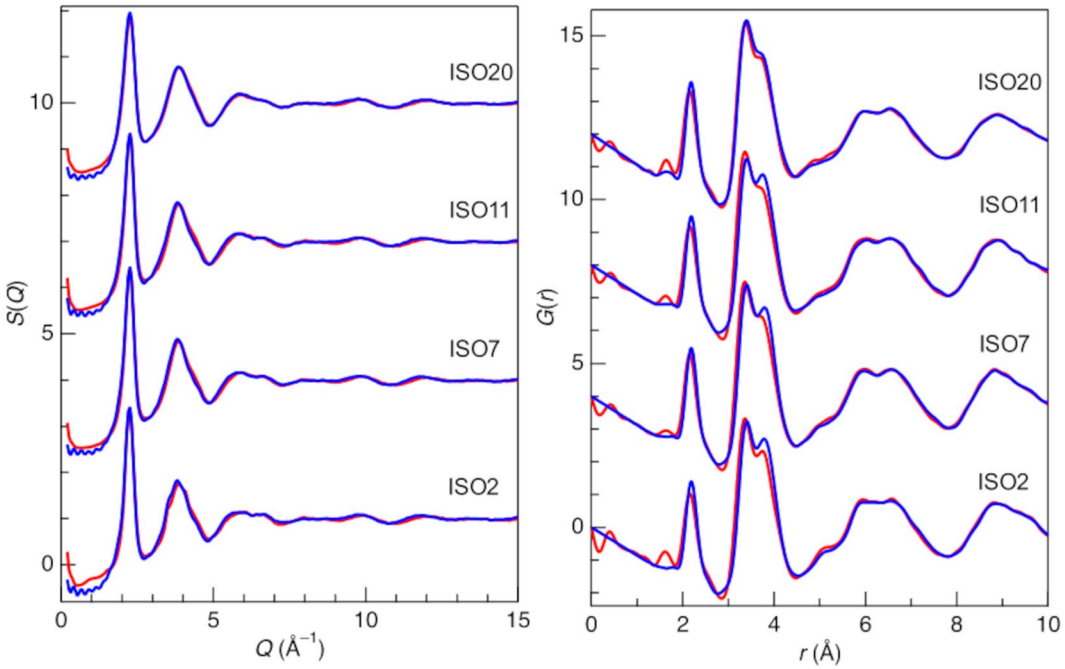


**Fig. 2**. X-ray total structure factors, $S(Q)$, and reduced pair distribution functions, $G(r)$, of pristine ISO together with the results of CMD–RMC modeling. Red line, experimental data; blue line, CMD–RMC model.

experimental and CMD–RMC data was significantly improved compared to the initial CMD model. Accordingly, we used the CMD–RMC model for further analysis.

All the $S(Q)$ of ISO exhibited nearly identical peaks, notably two prominent peaks at approximately $Q = 2.25$ Å$^{-1}$ and 3.85 Å$^{-1}$. A conventional oxide $SiO_2$ glass showed two distinct peaks at approximately $Q_1 \sim 1.50$ Å$^{-1}$ (first sharp diffraction peak) and $Q_3 \sim 5.20$ Å$^{-1}$ in the $S(Q)$, along with a significant oscillation at high $Q$ attributed to the formation of $SiO_4$ tetrahedra[47]. Although both ISO and $SiO_2$ exhibited similar peaks, the first peak of ISO appeared sharper than that of $SiO_2$. Intriguingly, the $S(Q)$ of ISO resembles those of $Zr_{70}Cu_{30}$ metallic glass and liquid Hg[48]. One notable similarity is the high packing density, which indicates that ISO is more similar to $Zr_{70}Cu_{30}$ metallic glass and the liquid Hg structure than to $SiO_2$ glass.

## Partial structural and short-range structural analysis of CMD–RMC models

Figure 3 shows the partial structure factors, $S_{ij}(Q)$, of ISO2, 7, 11, and 20. Notably, the Si–Si correlation does not clearly exhibit peaks owing to the small fraction of Si atoms. The cation–oxygen $S_{ij}(Q)$ ($S_{In-O}(Q)$ and $S_{Si-O}(Q)$) exhibits a negative peak at approximately $Q \sim 2.30$ Å, while the cation–cation $S_{ij}(Q)$ ($S_{In-In}(Q)$ and $S_{In-Si}(Q)$) and $S_{O-O}(Q)$ exhibit a positive peak. The negative peaks in the cation–oxygen correlations indicate that the cation was located at the center of the oxygen polyhedron. In contrast, Yu reported[49] a glass structure of $BaTi_2O_5$ showing positive cation–oxygen correlation peaks because the Ba atoms occupy off-center sites in the Ba–O polyhedra. In addition, the peak observed at approximately $Q \sim 2.36$ Å$^{-1}$ in the $S_{OO}(Q)$ shifts to a higher $Q$ region with the addition of $SiO_2$, which attribute to density changes.

Figure 4 shows the partial pair distribution functions, $g_{ij}(r)$, for ISO2, 7, 11, and 20 from the CMD–RMC modeling. No significant differences were observed with the addition of $SiO_2$. This result is crucial for understanding the thermal stability of ISO because it suggests that Si doping does not have a significant effect on structural changes. In other words, the structural changes induced by Si doping are not the origin of the ISO thermal stability. The features observed for $g_{In-In}(r)$ and $g_{O-O}(r)$ are particularly interesting. The $g_{In-In}(r)$ from 2.50 to 4.00 Å shows two peaks, while $g_{O-O}(r)$ exhibits tiny peaks at approximately 4.20 Å. Figure 5 illustrates the polyhedral connectivity of $InO_x$–$InO_x$ with corner and edge sharing. The $g_{In-In}(r)$ at approximately 3.20 Å and 3.90 Å indicate corner and edge-sharing of $InO_x$–$InO_x$. In addition, the small peaks of $g_{O-O}(r)$ indicate an oxygen–oxygen correlation on the diagonal of the oxygen polyhedron.

## Topological analysis

Figure 6 shows the In–In, In–O, and O–O coordination number distributions, and Table 3 presents the average coordination numbers for the ISO. Notably, the In–O and O–O data include two types of analyses, one of which excludes $SiO_4$ tetrahedra from the structural models (denoted by blue bars), as they are not relevant to the crystallization of ISO. Figure 7 shows the $InO_5$ polyhedron and $SiO_4$ tetrahedra. We counted only the bridging oxygens of –In–O–In–, excluding the oxygen atoms of the $SiO_4$ tetrahedra. The coordination number of the In–O-containing $SiO_4$ tetrahedra approaches that of the crystal structure ($N_{In-O} = 6$) with increasing Si content. This implies that the addition of $SiO_2$ facilitates crystallization but hinders the thermal stability of ISO. In contrast, in

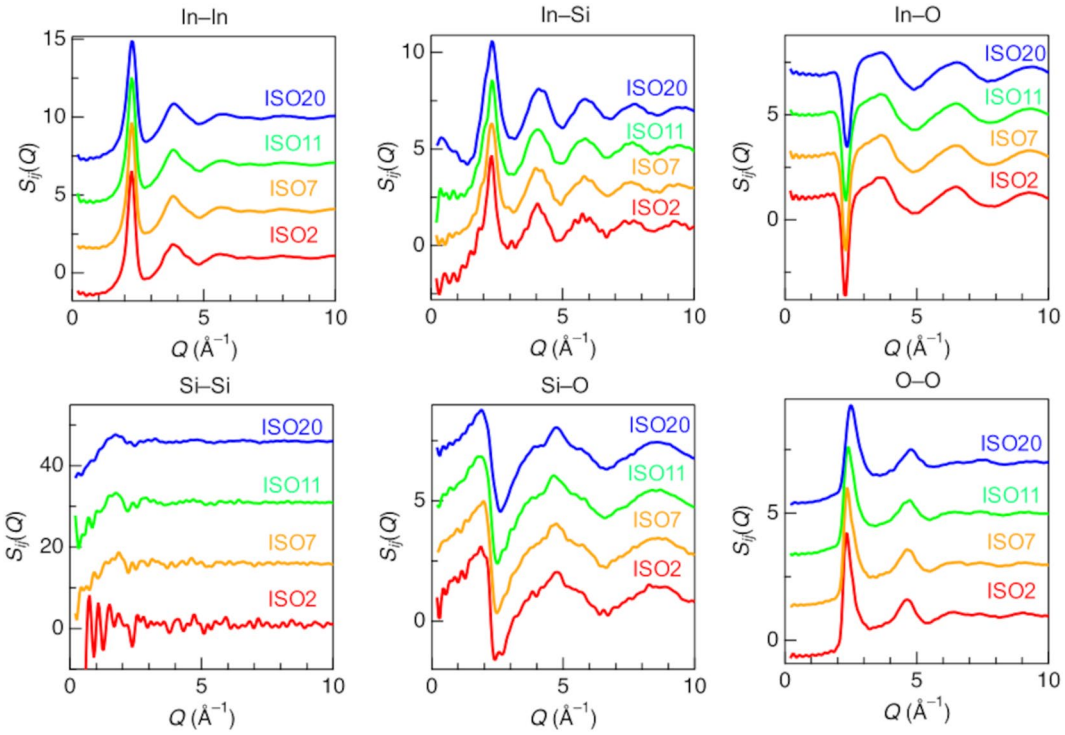


**Fig. 3**. Partial structure factors, $S_{ij}(Q)$, of pristine ISO2, 7, 11, and 20. Red line, ISO2; orange line, ISO7; green line, ISO11; blue line, ISO20.

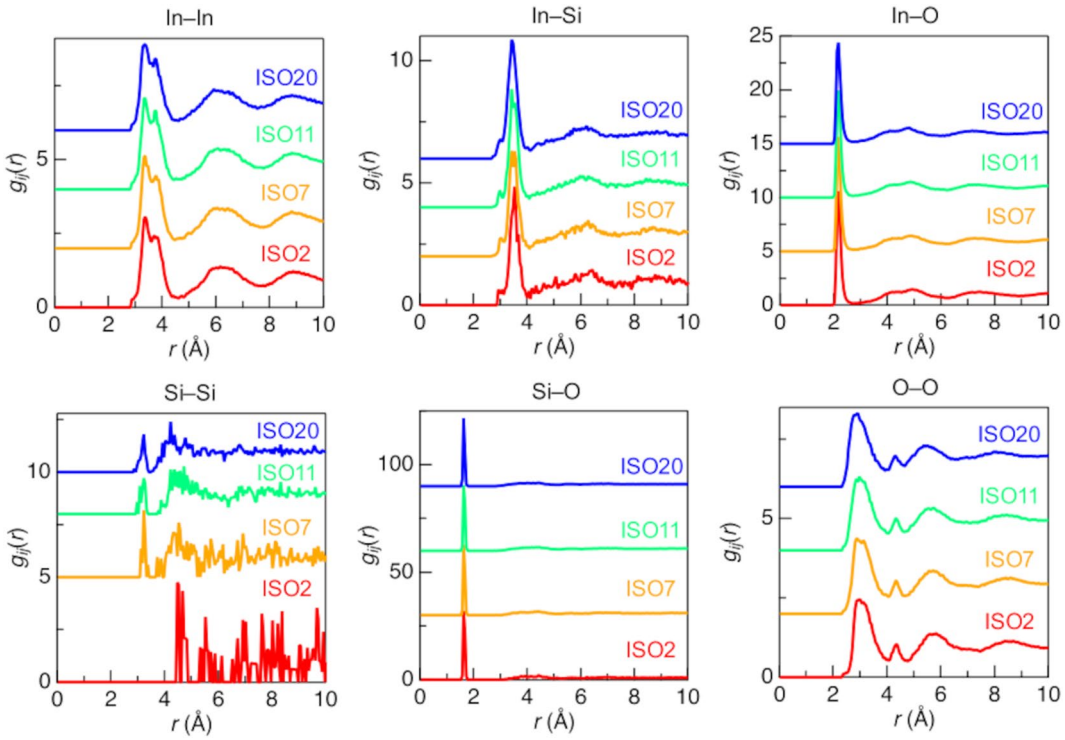


**Fig. 4**. Partial pair distribution functions, $g_{ij}(r)$, of pristine ISO2, 7, 11, and 20. Red line, ISO2; orange line, ISO7; green line, ISO11; blue line, ISO20.

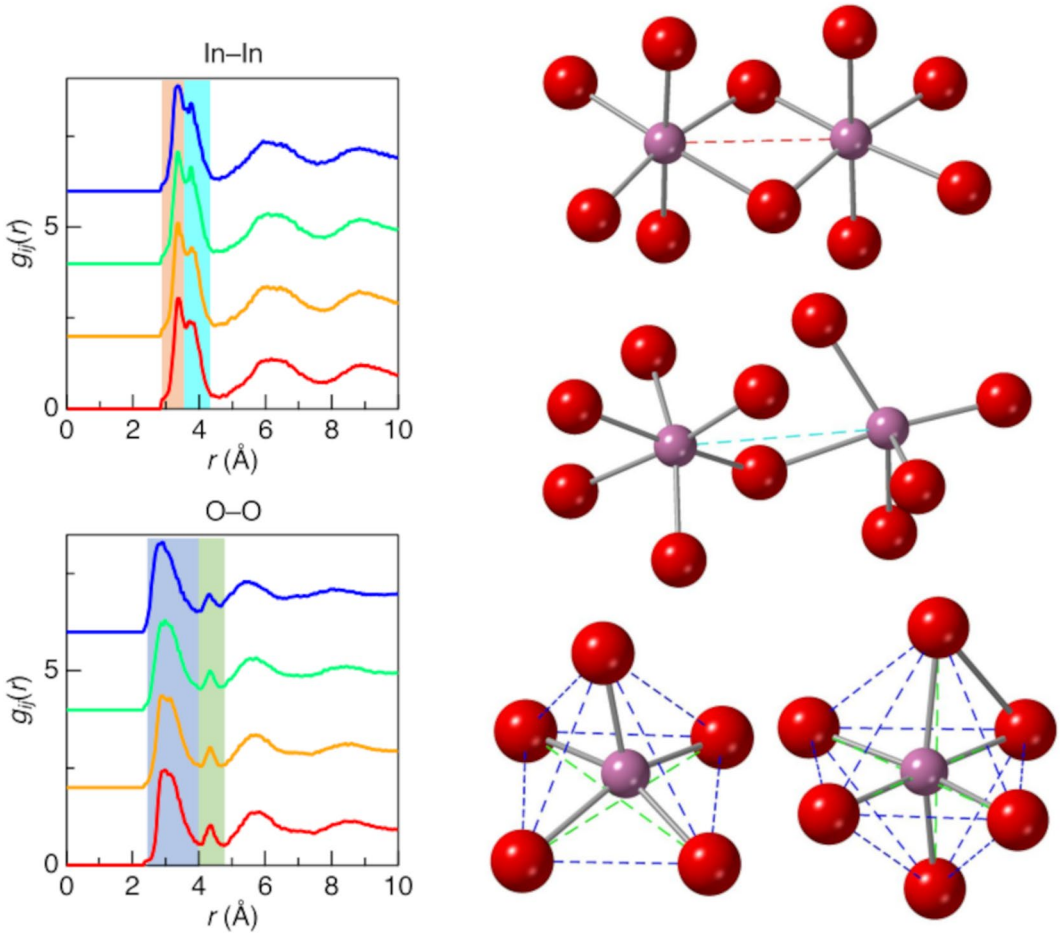


**Fig. 5**. Comparison between the partial pair distribution function, $g_{ij}(r)$, of In–In and O–O correlation and illustration of $InO_x$–$InO_x$ polyhedral connectivity. The red region and dotted line indicates the edge-sharing In–In interatomic distance, the cyan region and dotted line indicates the corner-sharing In–In interatomic distance, the blue region and dotted line indicates the nearest neighbor O–O distance, and the green region and dotted line indicates the diagonal O–O distance.

the $N_{In-O}$ without $SiO_4$ tetrahedra, the addition of Si led to broader peaks and decreased coordination numbers. This phenomenon is similar to that observed in amorphous materials[23,26].

Figure 8 shows the ring size distribution of crystalline $In_2O_3$ and ISO2, 7, 11, and 20. Four-fold rings were predominant in crystalline $In_2O_3$. Cooper reported that $SiO_2$ glass exhibits a wide distribution of rings, including large-fold rings[50]. Therefore, the dominance of four-fold rings in crystalline $In_2O_3$ indicates that this material is densely packed. All ring size distributions, except that for ISO20, show broad distributions owing to Si doping, but no significant differences between those with and without $SiO_4$ tetrahedra were observed. ISO20, with and without $SiO_4$, shows small differences, but both sets of data exhibit broad peaks, and the number of large rings increases. These results indicate that the thermal stability of ISO cannot be determined from structural information related to the intermediate- and long-range orders.

Table 4 summarizes the connectivity between $InO_x$–$SiO_4$ and $InO_x$–$InO_x$. All ISOs were within the corner-sharing motif for $InO_x$–$SiO_4$, although small fractions of edge-sharing polyhedra were observed. $SiO_4$ tetrahedra are well-known 100% corner-sharing in $SiO_2$ glass, which is a typical glass-forming oxide, and $SiO_4$ of ISO exhibits similar behavior. The $InO_x$–$InO_x$ connectivities with $SiO_4$ in ISO show a corner-sharing motif, but the fraction of edge-sharing polyhedra increases. In particular, $InO_x$–$InO_x$ for $c$-$In_2O_3$ exhibited 50% edge sharing. Koyama et al.[21] reported that $Er_2O_3$ liquid, which is classified as a non-glass-forming oxide, exhibits a large fraction of edge-sharing $ErO_n$ polyhedra. Based on this behavior, we conclude that the fraction of edge-sharing $InO_x$–$InO_x$ is the most crucial factor in understanding the crystallization of ISO. The fraction of edge-sharing $InO_x$–$InO_x$ with $SiO_4$ shows almost the same value, suggesting that changing the number of Si atoms has no effect on the thermal stability of ISO. To reconsider this contradiction, we compared the fractions of edge-sharing $InO_x$–$InO_x$ with and without $SiO_4$. The fraction of edge-sharing $InO_x$–$InO_x$ without $SiO_4$ decreased with Si doping. The dissociation energy of the Si–O bond was 799 kJ/mol, whereas that of the In–O bond was 346 kJ/mol[51], indicating that the Si–O bond had stronger connectivity than the In–O bond. This suggests that the $SiO_4$ tetrahedra of ISO are not broken down by the In–O bonds. Based on these results, we interpret the thermal

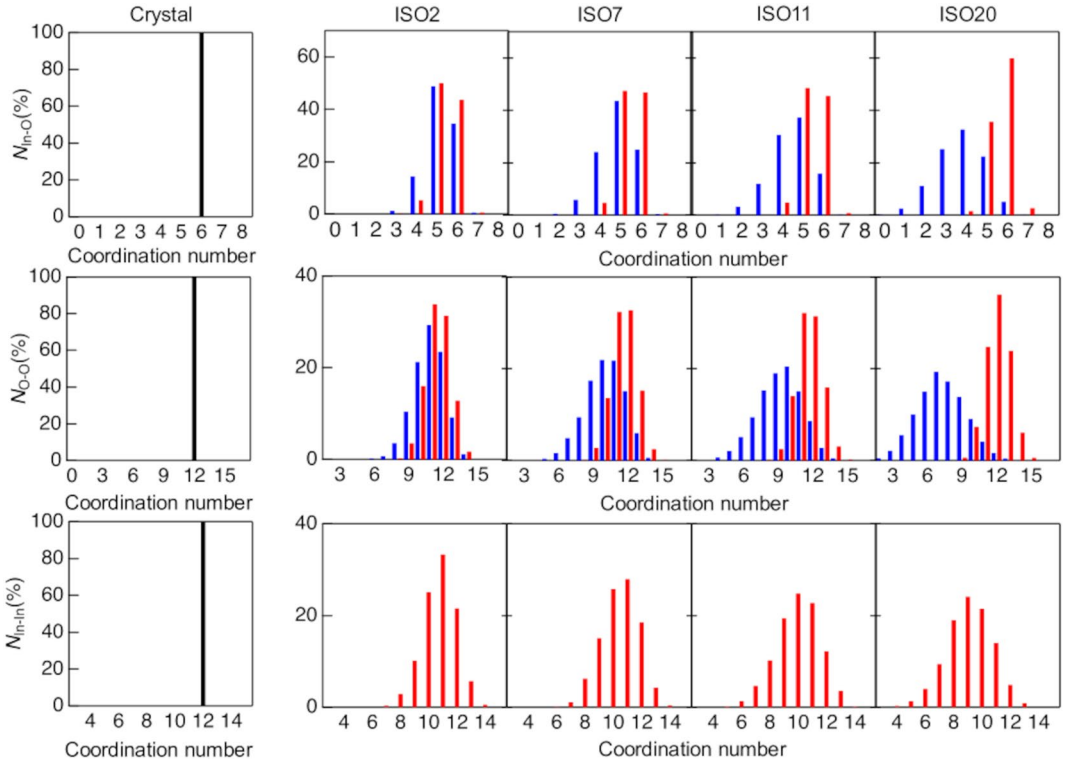


**Fig. 6**. Coordination number distributions of crystalline $In_2O_3$ and pristine ISO2, 7, 11, and 20. Black bar, crystalline; red line, ISO with $SiO_4$ tetrahedra; blue line, ISO without $SiO_4$ tetrahedra.

| | Crystal | ISO2 | ISO7 | ISO11 | ISO20 |
|---|---|---|---|---|---|
| With $SiO_4$ | | | | | |
| In–O | 6.00 | 5.39 | 5.44 | 5.42 | 5.64 |
| O–O | 12.00 | 11.39 | 11.52 | 11.54 | 11.97 |
| In–In | 12.00 | 10.79 | 10.48 | 9.98 | 9.11 |
| Si–O | – | 4.00 | 4.00 | 4.00 | 4.00 |
| Without $SiO_4$ | | | | | |
| In–O | 6.00 | 5.19 | 4.89 | 4.51 | 3.77 |
| O–O | 12.00 | 10.89 | 10.12 | 9.28 | 7.36 |
| In–In | 12.00 | 10.79 | 10.48 | 9.98 | 9.13 |

**Table 3**. Average coordination numbers of crystalline $In_2O_3$ and pristine ISO2, 7, 11, and 20 with and without $SiO_4$ tetrahedra.

stability of ISO to be derived from the strong covalent bonds of $SiO_4$ tetrahedra maintaining their configuration, and the $SiO_4$ tetrahedra prevent the formation of edge-sharing $InO_x$–$InO_x$ during annealing treatment.

## Conclusions

In this article, we discuss the relationship between the atomic structure and thermal stability of Si-doped amorphous $In_2O_3$. X-ray $S(Q)$ and $G(r)$ clarify the atomic distances, revealing that pristine samples of ISO2, 7, 11, and 20 exhibit an amorphous structure, whereas ISO, except ISO20, crystalizes after annealing at 600 °C. Moreover, the atomic correlation peaks of the Si-doped sample did not significantly change in real space. Combining CMD and RMC in a simulation allows us to perform a more precise structural modeling of the ISO compared to the CMD simulation alone. The $S(Q)$ of the ISO samples is more similar to those of $Zr_{70}Cu_{30}$ metallic glass and Hg liquid than that of $SiO_2$ glass because of the densely packed structure in ISO. The In–O coordination number distribution broadened in the atomic configuration of the ISO without $SiO_4$ tetrahedra with increasing Si content. Analysis of the polyhedral connectivity revealed that the majority of the connectivity of the $SiO_4$ tetrahedra is corner-sharing with the $InO_x$ polyhedra. In addition, the edge-sharing of $InO_x$–$InO_x$ without $SiO_4$ tetrahedra decreases with increasing Si doping. We conclude that the maintenance of

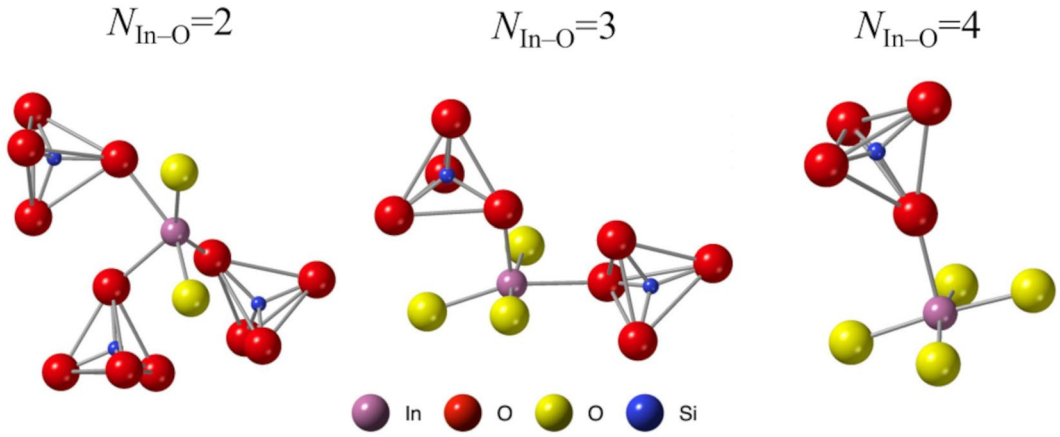


**Fig. 7**. Typical polyhedral arrangements of a $InO_5$ polyhedron and $SiO_4$ tetrahedra.

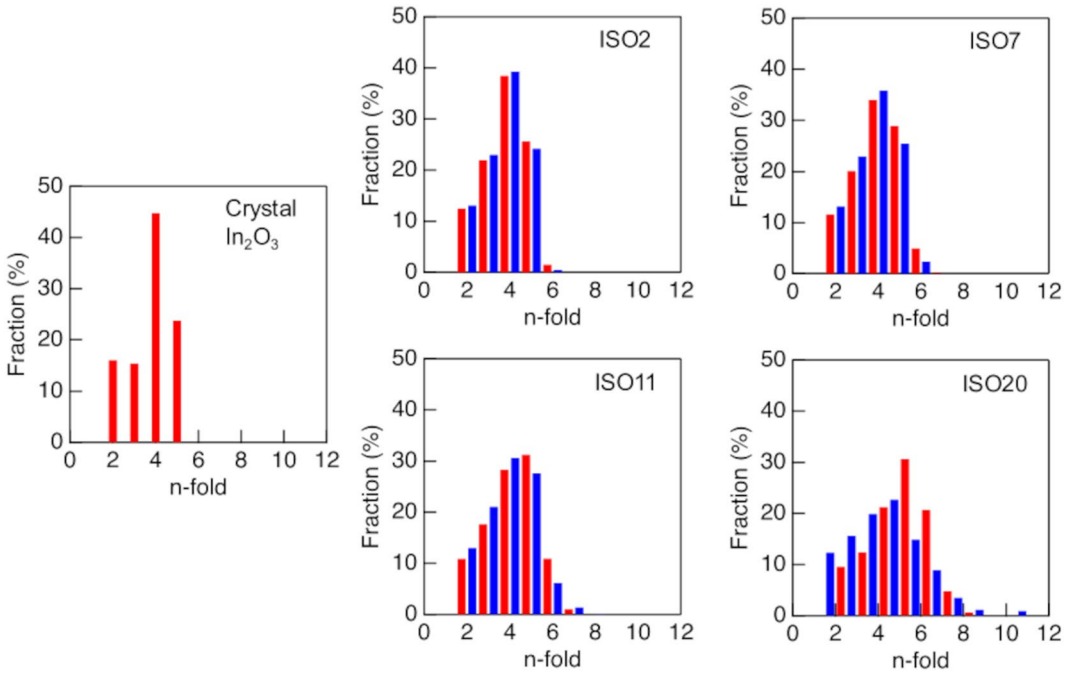


**Fig. 8**. Kings ring size distribution for crystalline $In_2O_3$ and pristine ISO2, 7, 11, and 20. Red line, crystalline $In_2O_3$ and ISO with $SiO_4$ tetrahedra; blue line, ISO without $SiO_4$ tetrahedra.

the amorphous structure of Si-doped ISO is attributed to the tolerance of $SiO_4$ tetrahedra formed by covalent bonds, preventing the formation of edge-sharing $InO_x$–$InO_x$ during heating treatment.

In this study, the structure of amorphous $In_2O_3$ was constructed using CMD simulations and then refined via RMC simulation to yield a model consistent with the experimental data. Recently, advances in high-precision methods of constructing potentials, including machine learning force fields (ML-FFs),[52] which enable the application of consistent potentials across different compositions, have been reported, and these methods may be effective in physically reasonable structural analyses. However, constructing the potential was beyond the scope of this study, and thus, RMC was adopted, focusing on practicality and consistency with the experimental results. In the future, improvements in CMD potentials and the introduction of ML-FFs should enable analyses using potentials that are consistent across all compositions.

These findings contribute to a better understanding of the role of Si doping in controlling the structural changes and properties of amorphous oxides. We believe that our findings will be crucial for various applications in optoelectronics and solid-state devices.

| | Corner | Edge | Face |
|---|---|---|---|
| $InO_x$–$SiO_4$ with $SiO_4$ | | | |
| ISO2 | 94.4 | 5.6 | 0.0 |
| ISO7 | 95.3 | 4.7 | 0.0 |
| ISO11 | 95.7 | 4.3 | 0.0 |
| ISO20 | 94.6 | 5.4 | 0.0 |
| $InO_x$–$InO_x$ with $SiO_4$ | | | |
| Crystal | 50.0 | 50.0 | 0 |
| ISO2 | 69.0 | 30.0 | 1.1 |
| ISO7 | 68.6 | 30.3 | 1.1 |
| ISO11 | 69.1 | 29.6 | 1.3 |
| ISO20 | 65.3 | 32.8 | 1.9 |
| $InO_x$–$InO_x$ without $SiO_4$ | | | |
| ISO2 | 70.1 | 28.9 | 1.0 |
| ISO7 | 71.7 | 27.5 | 0.8 |
| ISO11 | 73.9 | 25.2 | 0.8 |
| ISO20 | 76.4 | 22.9 | 0.7 |

**Table 4**. Polyhedral connectivity in crystalline $In_2O_3$ and pristine ISO2, 7, 11, and 20 with and without $SiO_4$ tetrahedra.

## Data availability

Data is provided within the manuscript or supplementary information files. The datasets used and/or analyzed during the current study available from the corresponding author on reasonable request.

Received: 1 April 2024; Accepted: 15 September 2025
Published online: 21 October 2025

## References

1. Markov, L. K. & Pavlyuchenko, A. S. & Smirnova I. P. Nanostructured ITO/$SiO_2$ coatings. *Semiconductors* **53**, 1033–1037 (2019).
2. Lee, S. J. et al. High-performance amorphous multilayered ZnO–$SnO_2$ heterostructure thin-film transistors: Fabrication and characteristics. *ETRI J.* **15**, 1135–1142 (2015).
3. Cho, S. Effects of rapid thermal annealing on the properties of $In_2O_3$ thin films grown on glass substrate by Rf reactive Magnetron sputtering. *Microelectron. Eng.* **89**, 84–88 (2012).
4. Wang, C. Y. et al. Growth mechanism and electronic properties of epitaxial $In_2O_3$ films on Sapphire. *J. Appl. Phys.* **110**, 093712 (2011).
5. Adurodija, F. O., Semple, L. & Brüning, R. Crystallization process and electro-optical properties of $In_2O_3$ and ITO thin films. *J. Mater. Sci.* **41**, 7096–7102 (2006).
6. Afre, R. A., Sharma, N., Sharon, M. & Sharon, M. Transparent conducting oxide films for various applications: A review. *Rev. Adv. Mater. Sci.* **53**, 79–89 (2018).
7. Roslyakov, I. V. et al. A Thin-film platform for chemical gas sensors. *Russ Electr. Eng.* **47**, 226–233 (2018).
8. Yu, X., Marks, T. J. & Facchetti, A. Metal oxides for optoelectronic applications. *Nat. Mater.* **15**, 383–396 (2016).
9. Morales-Masis, M. et al. Low-temperature high-mobility amorphous IZO for silicon heterojunction solar cells. *IEEE J. Photovolt.* **5**, 1340–1347 (2015).
10. Paine, D. C., Yaglioglu, B., Beiley, Z. & Lee, S. Amorphous IZO-based transparent thin film transistors. *Thin Solid Films.* **516**, 5894–5898 (2008).
11. Nomura, K. et al. Room-temperature fabrication of transparent flexible thin-film transistors using amorphous oxide semiconductors. *Nature* **432**, 488–492 (2004).
12. Kamiya, T. & Hosono, H. Material characteristics and applications of transparent amorphous oxide semiconductors. *NPG Asia Mater.* **2**, 15–22 (2010).
13. Kamiya, T., Nomura, K. & Hosono, H. Present status of amorphous In–Ga–Zn–O thin-film transistors. *Sci. Technol. Adv. Mater.* **11**, 044305 (2010).
14. Mitoma, N. et al. Stable amorphous $In_2O_3$-based thin-film transistors by incorporating $SiO_2$ to suppress oxygen vacancies. *Appl. Phys. Lett.* **104**, 102103 (2014).
15. Mitoma, N. et al. Dopant selection for control of charge carrier density and mobility in amorphous indium oxide thin-film transistors: Comparison between Si- and W-dopants. *Appl. Phys. Lett.* **106**, 042106 (2015).
16. Jan, H. E. et al. Amorphous In-Si-O films fabricated via solution processing. *J. Electron. Mater.* **46**, 3610–3614 (2017).
17. Mitoma, N. et al. Phase transitions from semiconductive amorphous to conductive polycrystalline in indium silicon oxide thin films. *Appl. Phys. Lett.* **109**, 221903 (2016).
18. Kohara, S. & Salmon, P. S. Recent advances in identifying the structure of liquid and glassy oxide and chalcogenide materials under extreme conditions: A joint approach using diffraction and atomistic simulation. *Adv. Phys: X.* **1**, 640–660 (2016).
19. Itoh, T. et al. Correlation among crystal and local structure, phase transition, and Li–ion conduction of solid electrolyte $Li_7La_3Zr_2O_{12}$. *J. Solid State Chem.* **327**, 124274 (2023).
20. Kitamura, N., Araki, Y., Ishida, N. & Idemoro, Y. Local structures in disordered rocksalt-type $Li_3NbO_4$-based positive electrode materials for a lithium-ion battery. *Phys. Status Solidi B.* **257**, 2000112 (2020).
21. Koyama, C. et al. Very Sharp diffraction peak in nonglass-forming liquid with the formation of distorted tetraclusters. *NPG Asia Mater.* **12**, 43 (2020).
22. Alderman, O. L. G. et al. Caotinuous structure transition in glass-forming molten titanate $BaTi_2O_5$. *J. Phys. Chem. C.* **120**, 26974–26985 (2016).

23. Shuseki, Y. et al. Structural analyses of amorphous calcium carbonate before and after removing strontium ions from an aqueous solution. *J. Ceram. Soc. Jpn.* **130**, 225–231 (2022).
24. Laaziri, K. et al. High resolution radial distribution function of pure amorphous silicon. *Phys. Rev. Lett.* **82**, 3460–3463 (1999).
25. Ohara, K., Onodera, Y., Murakami, M. & Kohara, S. Structure of disordered materials under ambient to extreme conditions revealed by synchrotron x-ray diffraction techniques at SPring-8–recent instrumentation and synergic collaboration with modelling and topological analyses. *J. Phys. Condens. Matter*. **33**, 383001 (2021).
26. Cormier, L., Hennet, L., Lelong, G., Cuello, G. J. & Bytchkov, A. Structure from glass to melt: A case study along the $MgSiO_3$–$CaSiO_3$ join using neutron and X-ray diffraction. *Comptes Rendus Géoscience*. **354**, 15–34 (2022).
27. Shuseki, Y. et al. Atomic and electronic structure in MgO–$SiO_2$. *J. Phys. Chem. A*. **128**, 716–726 (2024).
28. Buchholz, D. B. et al. The structure and properties of amorphous indium oxide. *Chem. Mater.* **26**, 5401–5411 (2014).
29. Aliano, A., Catellani, A. & Cicero, G. Characterization of amorphous $In_2O_3$: An Ab initio molecular dynamics study. *Appl. Phys. Lett*. **99**, 211913 (2011).
30. Kono, Y. et al. Experimental evidence of tetrahedral symmetry breaking in $SiO_2$ glass under pressure. *Nat. Commun.* **13**, 2292 (2022).
31. Hosokawa, S., Pilgrim, W. C., Bérar, J. F. & Kohara, S. Recent developments of anomalous X-ray scattering for non-crystalline materials with help of reverse Monte Carlo modeling: The example of $GeSe_2$ glass. *Phys. Status Solidi A*. **208**, 2544–2551 (2011).
32. Kawamata, T., Yokoyama, Y., Saito, M., Sugiyama, K. & Waseda, Y. Structural study of $Zr_{50}Cu_{50}$ amorphous alloy by anomalous X-ray scattering coupled with reverse Monte-Carlo simulation. *Mater. Trans.* **51**, 1796–1801 (2010).
33. Kohara, S. et al. Synchrotron X-ray scattering measurements of disordered materials. *Z. Phys. Chem.* **230**, 339–368 (2016).
34. Faber, T. E. & Ziman, J. M. A theory of the electrical properties of liquid metals. *Philos. Mag.* **11**, 153–173 (1965).
35. Antipas, G. S. E. & Karalis, K. T. Direct determination of amorphous number density from the reduced pair distribution function. *MethodsX* **6**, 601–605 (2019).
36. Tosi, M. P. & Fumi, F. G. Ionic ionic sizes and born repulsive parameters in the NaCl-type alkali halides—II: The generalized Huggins-Mayer form. *J. Phys. Chem. Solids*. **25**, 45–52 (1964).
37. Utsuno, F. et al. Structural study of amorphous $In_2O_3$ film by grazing incidence X-ray scattering (GIXS) with synchrotron radiation. *Thin Solid Films*. **496**, 95–98 (2006).
38. Zhang, Z., Xie, B., Zhou, W., Diao, J. & Li, H-Y. Structural characterization of FeO–$SiO_2$–$V_2O_3$ slags using molecular dynamics simulations and FT-IR spectroscopy. *ISIJ Int.* **5**, 828–834 (2016).
39. Ide, K., Nomura, K., Hiramatsu, H., Kamiya, T. & Hosono, H. Structural relaxation in amorphous oxide semiconductor a-In-Ga-Zn-O. *J. Appl. Phys.* **111**, 073513 (2012).
40. Plimpton, S. Fast Paralle algorithms for short-range molecular dynamics. *J. Comput. Phys.* **117**, 1–19 (1995).
41. Gereben, O., Jóvári, P., Temleitner, L. & Pusztai, L. A new version of the RMC++, reverse Monte Carlo programme, aimed at investigating the structure of covalent glasses. *J. Optoelectron. Adv. Mater.* **9**, 3021–3027 (2007).
42. Roux, S. L. & Jund, P. Ring statistics analysis of topological networks: New approach and application to amorphous $GeS_2$ and $SiO_2$ systems. *Comput. Mater. Sci.* **49**, 70–83 (2010).
43. Farrow, C. L. et al. PDFfit2 and pdfgui: Computer programs for studying nanostructure in crystals. *J. Phys.: Condens. Matter*. **19**, 335219 (2007).
44. Umemoto, K. & Wentzcovitch, R. M. Effect of the d electrons on phase transitions in transition-metal sesquioxides. *Phys. Chem. Minerals*. **38**, 387–395 (2011).
45. González, G. B. et al. Neutron diffraction study on the defect structure of indium–tin–oxide. *J. Appl. Phys*. **89**, 2550–2555 (2001).
46. Kapow, R., Strong, S. L. & Averbach, B. L. Radial density functions for liquid mercury and lead. *Phys. Rev.* **138**, A1336–A1345 (1965).
47. Onodera, Y. et al. Structure and properties of densified silica glass: Characterizing the order within disorder. *NPG Asia Mater.* **12**, 85 (2020).
48. Masuno, A., Kohara, S., Hannon, A. C., Bychkov, E. & Inoue, H. Drastic connectivity change in high refractive index lanthanum niobate glasses. *Chem. Mater.* **25**, 3056–3061 (2013).
49. Yu, L. et al. Comprehensive structural study of glassy and metastable crystalline $BaTi_2O_5$. *Chem. Mater.* **21**, 259–263 (2009).
50. Gupta, P. K. & Cooper, A. R. Topologically disordered networks of rigid polytopes. *J. Non-Cryst. Solids* **123**, 14–21 (1990).
51. Hoang, H. et al. Silicon-doped indium oxide – a promising amorphous oxide semiconductor material for thin-film transistor fabricated by spin coating method. *IOP Conf. Ser.: Mater. Sci. Eng.* **625**, 012002 (2019).
52. Erhard, L. C., Rohrer, J., Albe, K. & Dernger, V. L. A machine-learned interatomic potential for silica and its relation to empirical models. *Npj Comput. Mater.* **8**, 90 (2022).


## Acknowledgements

A part of this study was financially supported by JSPS KAKENHI (Grant Numbers: 24K17502), and Takahashi Industrial and Economic Research Foundation. Synchrotron radiation experiments were performed at SPring-8 with the approval of the Japan Synchrotron Radiation Research Institute (JASRI) (Proposal nos. 2015A1884 and 2016A1216). The calculations in this study were performed on the Numerical Materials Simulator at NIMS.

## Author contributions

S.K. designed the study. N.M., T.K., T.N., K.T., and A.F. prepared samples. T.K., K.T., A.F., K.O., and S.K. performed X-ray diffraction measurements. Y.S., Y.O. and A.M. conducted data analysis and computer simulations. Y.S. and S.K. wrote the manuscript with comments provided by all the authors.

## Declarations

## Competing interests

The authors declare no competing interests.

## Additional information

**Supplementary Information** The online version contains supplementary material available at https://doi.org/10.1038/s41598-025-20384-0.

**Correspondence** and requests for materials should be addressed to A.F. or S.K.

**Reprints and permissions information** is available at www.nature.com/reprints.

**Publisher's note** Springer Nature remains neutral with regard to jurisdictional claims in published maps and institutional affiliations.

**Open Access** This article is licensed under a Creative Commons Attribution 4.0 International License, which permits use, sharing, adaptation, distribution and reproduction in any medium or format, as long as you give appropriate credit to the original author(s) and the source, provide a link to the Creative Commons licence, and indicate if changes were made. The images or other third party material in this article are included in the article's Creative Commons licence, unless indicated otherwise in a credit line to the material. If material is not included in the article's Creative Commons licence and your intended use is not permitted by statutory regulation or exceeds the permitted use, you will need to obtain permission directly from the copyright holder. To view a copy of this licence, visit http://creativecommons.org/licenses/by/4.0/.

© The Author(s) 2025